2015

Hybrid Carbon Fiber Alumina Nanocomposite for Non-Contact Stress Sensing Via Piezospectroscopy

Imad Hanhan
University of Central Florida

HYBRID CARBON FIBER ALUMINA NANOCOMPOSITE FOR NON-CONTACT STRESS SENSING VIA PIEZOSPECTROSCOPY

by

Imad A. Hanhan

A thesis submitted in partial fulfillment of the requirements
for the Honors in the Major Program in Mechanical Engineering
in the College of Engineering and Computer Science
at the University of Central Florida
Orlando, Florida

Spring Term, 2015

Major Professor: Seetha Raghavan

Abstract

Carbon fiber composites have become popular in aerospace structures and applications due to their light weight, high strength, and high performance. Recently, scientists have begun investigating hybrid composites that include fibers and particulate fillers, since they allow for advanced tailoring of mechanical properties, such as improved fatigue life. This project investigated a hybrid carbon fiber reinforced polymer (HCFRP) that includes carbon fiber and additional alumina nanoparticle fillers, which act as embedded nano stress-sensors. Utilizing the piezospectroscopic effect, the photo-luminescent spectral signal of the embedded nanoparticles has been monitored as it changes with stress, enabling non-contact stress detection of the material. The HCRFPs stress-sensitive properties have been investigated *in-situ* using a laser source and a tensile mechanical testing system. Hybrid composites with varying mass contents of alumina nanoparticles have been studied in order to determine the effect of particle content on the overall stress sensing properties of the material. Additionally, high resolution photo-luminescent maps were conducted of the surfaces of each sample in order to determine the particulate dispersion of samples with varying alumina content. The dispersion maps also served as a method of quantifying particulate sedimentation, and can aid in the improvement of the manufacturing process. The results showed that the emitted photo-luminescent spectrum can indeed be captured from the embedded alumina nanoparticles, and exhibits a systematic trend in photo-luminescent peak shift with respect to stress. The stress maps

showed a linear increase in peak shift up to a certain critical stress, and matched closely with the DIC strain results. Therefore, the non-contact stress sensing results shown in this work have strong implications for the future of structural health monitoring and nondestructive evaluation (NDE) of aerospace structures.

Dedication

This work is dedicated to my mother and father; without your unconditional love and support, I would not be where I am today.

Acknowledgments

I would like to thank my advisor Dr. Seetha Raghavan for her guidance in my thesis project, her mentorship and overall support throughout my undergraduate research efforts at the University of Central Florida (UCF), and for all the research opportunities she has provided me. Thank you to my thesis committee members, Dr. Jihua Gou and Dr. Yuanli Bai for their support in this thesis. I would also like to thank all the members of my research team, specifically Dr. Gregory Freihofer and Alex Selimov, who helped me with different aspects of this work.

I would like to acknowledge Dr. Ambrose Taylor and Dr. Declan Carolan from Imperial College London for their collaborative contribution in manufacturing the materials studied in this work. Additionally, I would like to acknowledge Dr. Yuanli Bai's research team for facilitating the Digital Image Correlation utilized in this study.

Thank you to the National Science Foundation's Innovation through Institutionalized Integration (ICubed) Fellowship, as well as the UCF Research and Mentorship Program (RAMP) for their support of my undergraduate research efforts. This material is based upon work supported by the National Science Foundation under Grant No 1130837, as well as a grant provided by the UCF Office of Undergraduate Research.

TABLE OF CONTENTS

LIST OF FIGURES

LIST OF TABLES

CHAPTER 1
INTRODUCTION

The future of aerospace structures is highly dependent on the advancement of reliable and high performing materials [69]. One group of high performing materials include carbon fiber composites, which have become widely used in aerospace applications due to their high strength to weight ratios [63]. Specifically, hybrid carbon fiber reinforced polymer (HCFRP) composites are a growing area of interest for aerospace researchers, since they provide advanced tailoring and improved mechanical properties [46, 71].

A certain hybrid composite can be engineered to not only provide improved mechanical properties, but also provide multi-functionality through inherent sensing capabilities. This composite is a hybrid carbon fiber alumina nano-composite, which can provide improvements in mechanical properties [40, 48, 2], as well as non-contact stress sensing capabilities through the alumina nanoparticles' inherent photo-luminescent piezospectroscopic properties [58, 65, 21].

In order to study the stress sensing abilities of the alumina HCFRP, four varying HCFRP panels were manufactured with alumina nanoparticles at 5, 10, 15, and 20 weight percent content, through a technique known as resin infusion under flexible tooling (RIFT). Rectangular testing coupons were then fixed with aluminum end tabs, and loaded in tension. At pre-determined static tensile holds, photo-luminescent maps were conducted on the front surface in order to study the piezospectroscopic stress sensing ability of the material, and digital image correlation (DIC) images were simultaneously

captured on the back surface to track and compare strain distribution in the material. The photo-luminescent mapping technique was also used to study the dispersion of nanoparticles of each surface of the composites [64].

1.1 Motivation and Background

Evaluating for damages is a crucial part of any aircraft's inspection and maintenance routine. Some of the most traditional non-destructive evaluation (NDE) methods are vibration based response techniques, often utilizing the response of a damaged structure with respect to and un-damaged structure [72, 66, 60]. Popular techniques also include ultrasound [15], thermography [6], and shearography [17].

While many of the mentioned techniques are widely used and provide accurate results, piezospectroscopy - an emerging non-contact technique for monitoring spectral emissions as they change with stress - can have benefits such as early damage detection and high spatial resolution. The non-contact stress sensing capability is made possible in this work by stress sensing alumina nanocomposites [65] and on-site portable equipment [34].

Previous work has proven that alumina nanoparticles can successfully be embedded in an epoxy matrix for non-invasive stress sensing [65]. This has led to the use of alumina nanoparticles as coatings for non-contact stress and damage detection [21, 19, 20], as well as the development of equipment specialized for photo-luminescent mapping, deconvolution, and post-processing of piezospectroscopic maps [34].

The basis of this sensing technique is the stress-sensitive photo-luminescent properties of alumina, which in this study, has been embedded as a nanoparticulate filler. When excited with a laser, the embedded alumina emits a signature spectrum that can be monitored as it shifts with stress. This is further explained in chapter 2.

The success of the piezospectroscopic alumina nanocomposite coatings in stress sensing and early damage detection led to this HCFRP study, which embedded the alumina nanoparticles into the composite for future applications in structural health monitoring, as can be seen in Figure 1.1. This approach has a number of benefits, including enhanced mechanical properties and improved manufacturing.

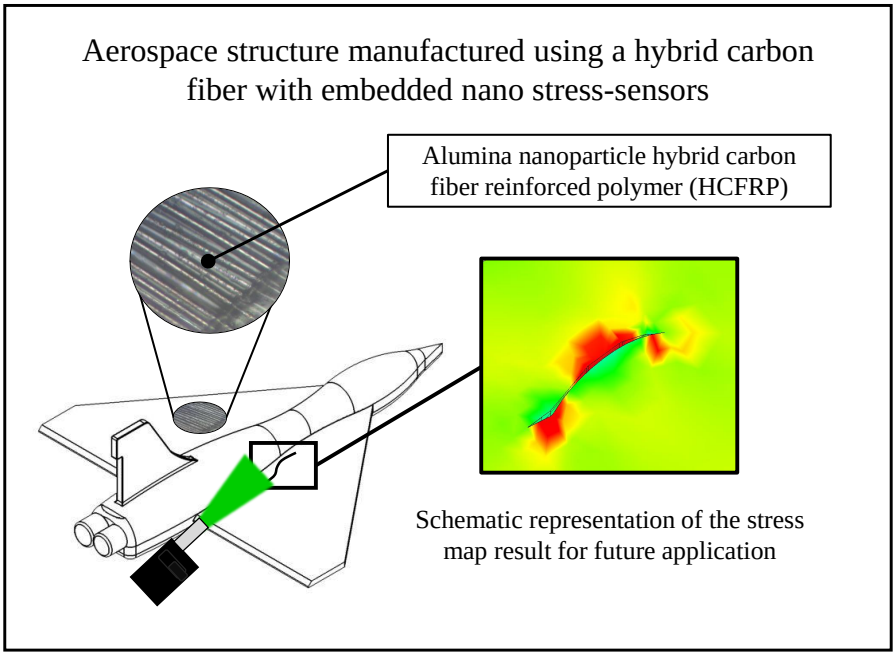

Figure 1.1: Future applications of stress sensing hybrid materials

1.1.1 Carbon Fiber Composites

Carbon based fillers in a polymer matrix have become used in many engineering fields, and can range from carbon nano-tube (CNT) composites to fibrous composites [52]. While the term 'carbon fiber' has become used almost universally to describe a composite with a polymer matrix and a carbon fiber filler, it is an umbrella term that encompasses different types of carbon fiber fillers.

For example, there are short carbon fiber thermoplastic (SFT) composites, which utilize small discontinuous carbon fibers, and have reduced mechanical strength but can be manufactured at low cost [3, 18, 25, 24, 26, 27]. On the other hand, there are long fiber thermoplastic (LFT) composites, which utilize long carbon fiber (typically 7-12 mm), and have slightly stronger mechanical properties [14, 51, 54, 55]. These short and long carbon fiber composites are typically molded using an injection molding technique [8, 18, 68] and while not suitable for aerospace applications, can be ideal for automotive applications [36].

For applications requiring the highest performing materials, such as aerospace applications, 'carbon fiber' composites typically refer to continuous carbon fiber laminates strategically organized in an epoxy matrix [37], which have become increasingly used in aerospace structures [63]. These exceptionally strong continuous fibrous composites have been of interest to researchers due to the complex nature of their performance, which includes their mechanical properties [70], their fiber-matrix interface properties [59], as well as causes of failure and failure modes [31, 9, 62].

Overall, carbon fiber composites have been proven to have light weight and high performance properties, especially as it pertains to aerospace applications [63]. Therefore, this study utilizes a unidirectional carbon fiber composite with additional modifications for toughening and advanced sensing.

1.1.2 Hybrid Composites

Fibrous composites can be customized by increasing or decreasing the volume fraction of the fiber content. While this allows for some modifications in performance, hybrid fibrous composites provide an even higher level of customizability, such as increased toughness and improved fatigue behavior [39, 46]. These hybrid materials often include a fibrous filler as well as a particulate filler(s).

A hybrid composite consisting of a carbon fiber filler and an additional particulate filler is commonly referred to as a hybrid carbon fiber reinforced polymer (HCFRP). In this work, a HCFRP which includes an alumina nanoparticle filler is studied for its stress sensing capabilities.

1.1.3 Alumina Particulate Composites

From a structural perspective, aluminum oxide (Al_2O_3) - or alumina - is a ceramic popular for its high temperature capabilities, and specifically, the retention of its mechanical strength at high temperatures [50, 28, 32].

Additionally, α-alumina exhibits a photo-luminescent spectrum that is sensitive to the stress the material sustains, a phenomenon known as the piezospectroscopic effect [45, 44]. Traditionally, the utilization of piezospectroscopy with alumina as a nondestructive evaluation technique was used in the study of the naturally forming alumina layer in thermal barrier coatings [11, 13, 57, 30, 42, 61].

Advancements have led to the integration of alumina nanoparticles into an epoxy matrix, resulting in a patented stress sensing technique capable of non-contact stress and damage detection [58, 65]. Additionally, successful early damage detection of materials with piezospectroscopic coatings [21, 20] has motivated using alumina nanoparticles as fillers in the HCFRP studied in this work.

CHAPTER 2
METHODS: PHOTO-LUMINESCENCE AND DIC

The methods used in this work, photo-luminescent spectroscopy and digital image correlation (DIC), are explained here.

2.1 Photo-luminescent Piezospectroscopy

Through the piezospectroscopic effect, certain photo-luminescent materials emit spectral peaks which are sensitive to the stress that the material sustains [16, 56, 29, 49, 44]. As previously mentioned, piezospectroscopic stress measurements have been utilized in the study of thermal barrier coatings [11, 13, 57, 30, 42, 61], however it has also historically been used to quantify pressure in a diamond-anvil cell [7, 10].

In this work, photo-luminescent spectroscopy and the piezospectroscopic effect are used to quantify the stress of a hybrid composite embedded with chromium (Cr^{3+}) doped polycrystalline α-Al_2O_3 nanoparticles. The intense fluorescence lines used in the piezospectroscopic stress analysis, referred to as R-lines, are due to the trace (Cr^{3+}) ions [33]. In the crystal structure, this trace (Cr^{3+}) is located at a site with a trigonal distortion. This distortion, as well as the spin-orbit coupling, results in doublet florescence peaks, known as R1 and R2 [38].

The piezospectroscopic effect for non-contact stress sensing of crystalline materials is based on the fact that an applied stress to the material produces strains in the lattice,

and therefore affects the energy transitions between electronic or vibrational states [45]. This phenomenon is governed by the tensorial relationship by Grabner [33]:

$$\Delta\nu = \Pi_{ij}\sigma^*_{ij} \tag{2.1}$$

where $\Delta\nu$ is the wavenumber (inverse of wavelength) shift in the fluorescent peak, Π_{ij} are piezospectroscopic coefficients, and σ^*_{ij} is the homogeneous stress applied to the material. Furthermore, by averaging over many grains at random orientation, He and Clarke [35] introduced a reduced polycrystalline model given by

$$\Delta\bar{\nu} = \frac{1}{3}\Pi_{ii}\sigma_{jj} \tag{2.2}$$

In this work, the peak shift over many randomly oriented grains from many nanoparticles, $\Delta\bar{\nu}$, is measured using the novel Portable Piezospectroscopy System [34], and correlated to the stress applied by the mechanical testing system, as well as to the strain measured via digital image correlation (DIC). Therefore, the piezospectroscopic (PS) coefficient, which is a typical measure of the stress sensitivity given in units of cm^{-1}/GPa, can be calculated for this alumina HCFRP [65, 22, 35].

2.2 Digital Image Correlation (DIC)

Digital image correlation (DIC) is an optical measurement technique used to detect surface displacements, which can be correlated to surface strains [12, 47]. DIC is typically made possible by a speckle pattern that is randomly painted on the surface of interest, creating bundles of pixels that can be monitored as the material deforms. By comparing digital images of a speckled surface at different stages of deformation, DIC is capable of creating strain maps of the surface of interest [47].

The ability of DIC to capture strain fields over a surface not only makes it more advantageous than traditional strain gages, but it also makes it a complementary measurement technique for piezospectroscopic stress-mapping. Therefore in this study, DIC was simultaneously used on the back surface of the stressed sample, while piezospectroscopic mapping was conducted on the front surface.

CHAPTER 3
SAMPLE MANUFACTURING AND EXPERIMENTATION

The manufacturing of the hybrid carbon fiber composite is explained here, as well as the overall experimental setup that enabled tensile testing with *in-situ* piezospectroscopic mapping and DIC strain mapping.

3.1 Sample Geometry and Manufacturing

The alumina HCFRP samples were manufactured at Imperial College London utilizing a technique known as resin infusion under flexible tooling (RIFT) to produce the hybrid continuous fiber-reinforced composites [39]. Through this method, a vacuum is used to inject the resin through the fibers and therefore achieves a composite free of voids. There are a number of advantages to using this technique of composite manufacturing, one being the higher fiber volume fraction capabilities.

In this study, uni-directional carbon fiber reinforced epoxy with embedded alumina nanoparticles was manufactured. The uni-directional carbon fiber used was 'RUCT500/150' from SP Systems, UK. The resin used was EPON^{TM} 862 and EPIKURE^{TM} Curing Agent.

Four hybrid composite panels were manufactured, each with a carbon fiber volume fraction of $57 \pm 3\%$, in a matrix of epoxy containing alumina nanoparticles at contents of 5, 10, 15, and 20 percent by weight, respectively. Rectangular testing coupons were

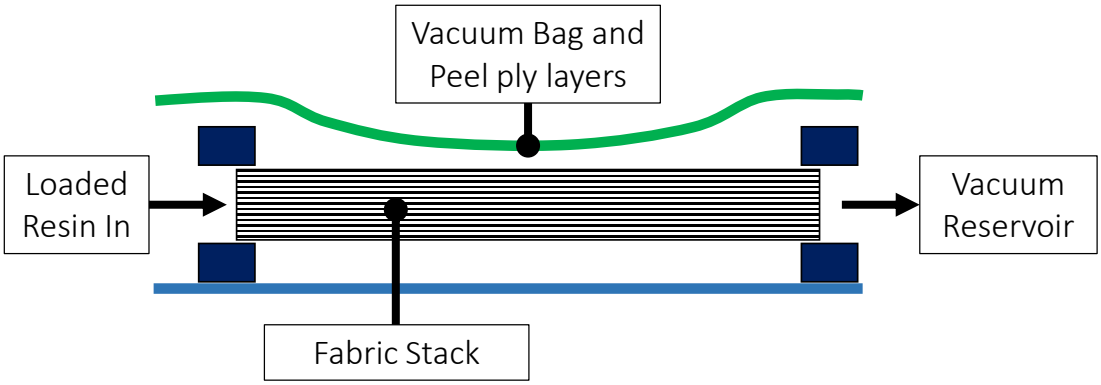

Figure 3.1: Schematic of the RIFT manufacturing process

then cut from the panels with dimensions of 100 by 10 mm, and an inherent thickness of 3 mm.

3.1.1 Alumina Particles

The α-alumina nanoparticles were provided as nanopowder from Inframat® Advanced Materials™, USA. The nano α-alumina had a purity of 99.85%, an average grain size of approximately 40 nm, an average particle size of 150 nm, and a multi-point surface area (SSA) of approximately 10 m^2/g, as per manufacturer specifications [41]. In the overall hybrid composite manufacturing process, the alumina particles are first embedded into the epoxy, which is then applied as the matrix to the uni-directional carbon fiber laminates.

3.1.2 End Tabs

End tabs can be a challenging aspect of tensile testing for composites. The ASTM D3039/D3039M guide (standard test methods for tensile properties of polymer matrix composite materials) explains that end tabs are not required, and are more of an art than a science [4]. Additionally, the use and choice of end tabs depends highly on the gripping methods of the sample [4, 5].

In this work, an MTS Insight Electromechanical system fitted with a 50 kN load cell was used. Specifically, the system utilized wedge grips with rough textured gripping teeth, ideal for metallic substrates. In order to improve gripping and to prevent sample slippage in the MTS grips, aluminum 6061 end tabs were cut from an aluminum sheet of thickness 3.175 mm, into dimensions of 1 cm by 2 cm. An example of a final sample can be seen in Figure 3.2.

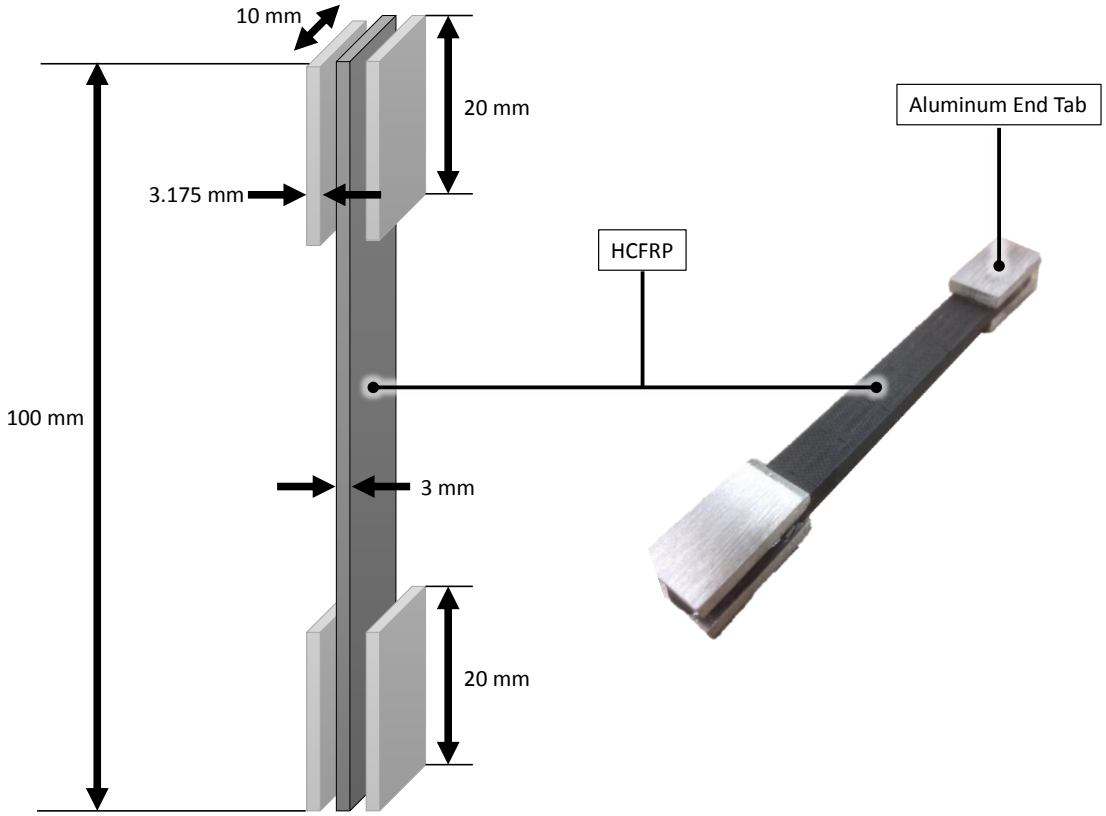

Figure 3.2: Final Samples

3.2 Experimental Setup

The experimental set-up and equipment used to conduct testing are described here.

3.2.1 Photo-Stimulated Luminescent Spectroscopy

The main system used for the non-contact stress sensing experiments is a novel and compact system named the Portable Piezospectroscopy System [34]. This system utilizes a spectrograph, a charge-coupled device (CCD), as well as a laser source and X-Y-Z stages, providing mapping capabilities, as can be seen in Figure 3.3. Additionally, this portable system has a computer used for data collection and deconvolution [34].

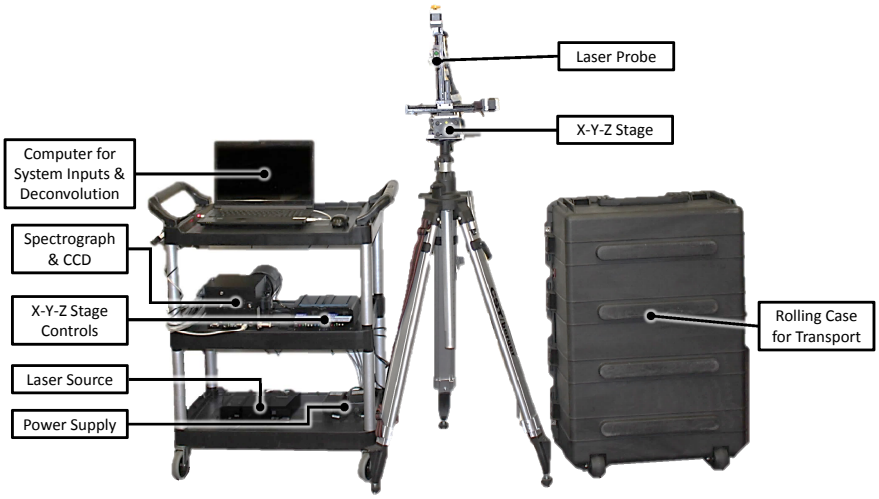

Figure 3.3: PPS System [34]

Furthermore, this system utilizes a a series of algorithms that filter the data using a signal-to-noise ratio, as well as solve a pseudo-Voigt curve fit to the spectral peaks, using a non-linear least squares curve fitting method. The final piezospectroscopic map contains an R-line signal peak shift captured in each pixel, which is then assigned a color, as can be seen in Figure 3.4.

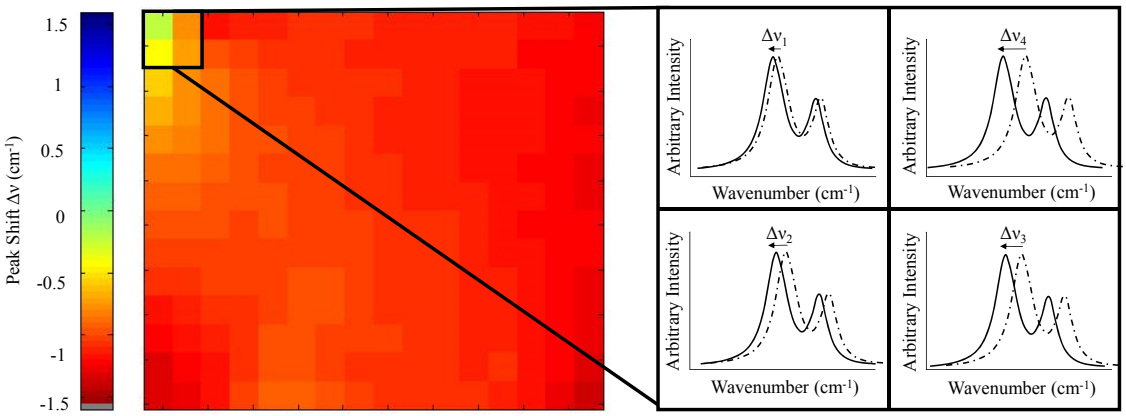

Figure 3.4: Piezospectroscopic mapping software output [34]

3.2.2 Tensile Testing Set-Up

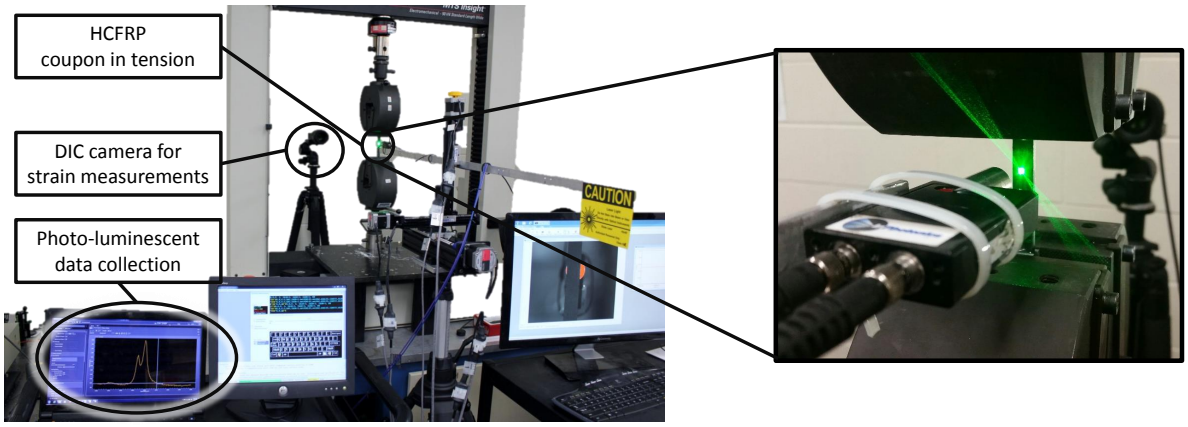

Figure 3.5: Overall experimental setup

In order to conduct tensile static holds of the samples, the MTS Insight Electromechanical system, with a calibrated 50 kN load cell was programmed to apply tensile static

holds at increments of 0.75 kN, or 25 MPa, up to a maximum load of approximately 400 MPa, as can be seen in Table 3.1. This load is about 30% of the estimated ultimate tensile strength [53]. At this load, the adhesive layer between the end tabs and sample failed. Therefore, future work should utilize a stronger, industrial-grade epoxy for end tab adhesion.

Prior to any loading, a zero load photo-luminescent (PL) map was conducted as the reference map. Then at each static tensile hold, a PL map was conducted, as well as a final PL map at zero load after the sample was unloaded back to 0 MPa. Simultaneously, DIC images were acquired during ramp up, as well as while the sample was held at a constant tensile force. The PL maps conducted in this part of the work had dimensions 1 cm by 1 cm, and spectral dimensions of of 20 by 20 pixels, resulting in a 500 μm resolution.

Table 3.1: Max tensile load per sample

Alumina Content	**Max Tensile Load Achieved**
5	450 MPa
10	425 MPa
15	375 MPa
20	320 MPa

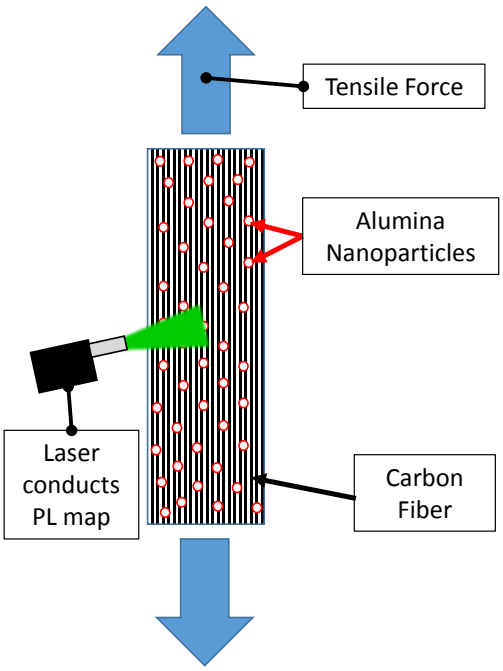

Figure 3.6: Schematic of tensile testing

One artifact of the combined photo-luminescent mapping and simultaneous DIC on the back of the sample is the potential interference of the laser with the DIC camera. In order to avoid any erratic DIC images due to the laser source, the laser probe was turned off during ramp up, and remained off for the first few seconds of a static hold. Then, after a number of DIC images were captured while the MTS is holding, the DIC camera was turned off, the laser probe was turned on, and a PL map was initiated. Once the PL map was complete, the laser probe was turned off, and the DIC camera was turned back on. At this point, the DIC camera collected a number of images until the tensile static hold ended, and the next load ramp up began.

Table 3.2: Tensile testing parameters

HCFRP	Exposure Time	Map Time	Tensile Hold Time	Number of PL Maps Achieved
5 wt% Alumina	350 ms	2 min 33 s	4 min	19
10 wt% Alumina	300 ms	2 min 13 s	4 min	18
15 wt% Alumina	200 ms	1 min 28 s	3 min	16
20 wt% Alumina	150 ms	1 min 13 s	3 min	15

Timing was clearly a critical factor in these experiments, as it was important to capture DIC strain images, while ensuring the PL maps could be acquired without interfering with the DIC camera, all while maintaining a tensile static hold. The specific parameters and times of acquisition for each sample can be seen in Table 3.2.

CHAPTER 4
PARTICULATE DISPERSION ANALYSIS

Particulate dispersion is an important characteristic of nanoparticulate composites, since it has direct relationships to the uniformity of the material and its mechanical properties. Characterizing particulate dispersion can also aid in improvements of the manufacturing techniques of hybrid composites. One of the benefits of using photo-luminescent spectroscopy to characterize dispersion is its high spatial resolution capabilities, which allow for a direct and detailed analysis of particulate dispersion.

4.1 High Resolution Photo-Luminescent Mapping

The same photo-luminescent properties that allow for non-contact stress sensing also allow for dispersion characterization of the composite material. It has been shown that the intensity of the spectral signal emitted from alumina nanoparticles can be used to characterize particulate dispersion [64]. It is important to note that the dispersion maps conducted on the samples are of the surface and near-subsurface of the material. Therefore, a high resolution photo-luminescent map was conducted on the front and back side of each sample, in order to not only observe dispersion properties, but also observe sedimentation properties of each sample.

Through visual inspection, the 15 and 20 weight percent samples appeared to have some particulate settling on one side, while the 5 and 10 weight percent samples did not

have visual differences on their front and back faces. In order to conduct a global study of all samples, the same exposure time and laser power was used. This not only enabled front to back comparisons of each sample, but also global sample-to-sample comparisons.

Prior to each dispersion map, the laser was focused onto the surface of the sample, and all necessary parameters were set in the PPS System [34], such as the map size and the spectral resolution. Relevant experimental parameters for the dispersion maps can be found in Table 4.1.

Table 4.1: Dispersion map parameters

Parameter	**Value**
Number of Samples	4 (one of each alumina content)
Coupon Dimensions	100 x 10 x 3 mm
Map Dimensions	12mm x 50 mm
Desired Resolution	200 μm
Spectral Map (X by Y)	60 by 250
Number of Maps	8 (front and back of 4)
Time per Map	90 minutes

4.1.1 Particulate Dispersion Results

As the laser probe is moved across the sample, the emitted spectrum from the embedded alumina nanoparticles was collected every 200 μm. The probe moved horizontally 12 mm across the sample's width, and then lowered down 200 μm to the next row and scanned back in the opposite horizontal direction. After mapping the specified region of interest (12 by 50 mm), the PPS System collected 15,000 R-line spectrum readings from the region of interest.

Therefore, each pixel has a corresponding R1 intensity, which fluctuates depending on the amount of alumina present at that location [64]. Each side of each sample was labeled either A or B, and below are the dispersion maps of each sample. The plotted color-bar maximum is the same for side A and side B of each sample, but is different for each sample in order to better observe dispersion per sample.

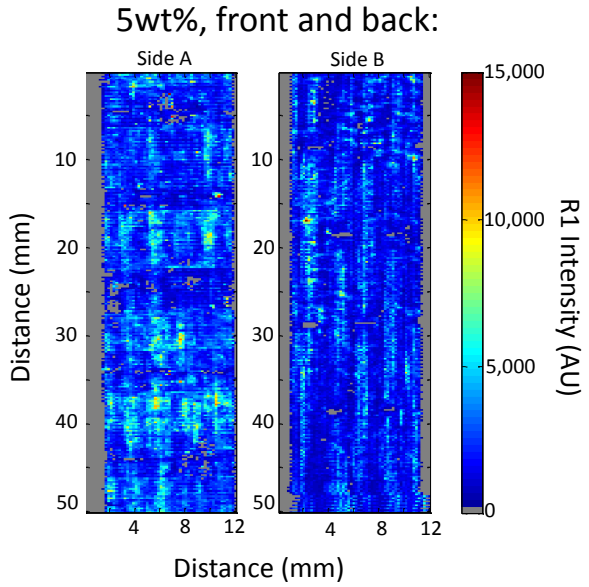

Figure 4.1: Dispersion maps of 5wt% alumina sample

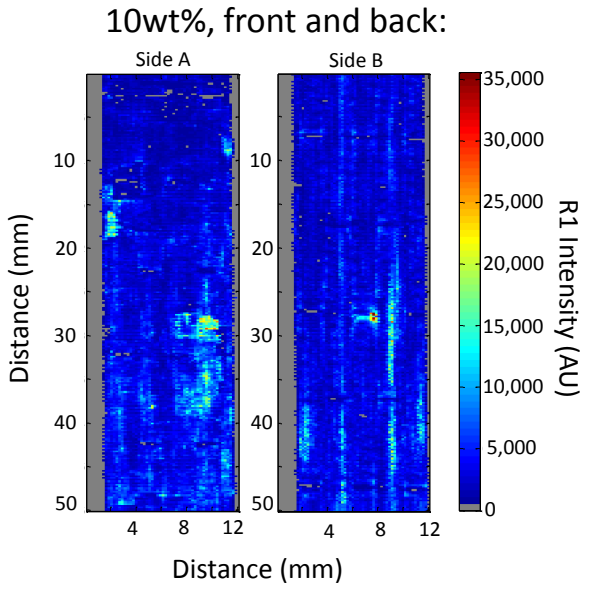

Figure 4.2: Dispersion maps of 10wt% alumina sample

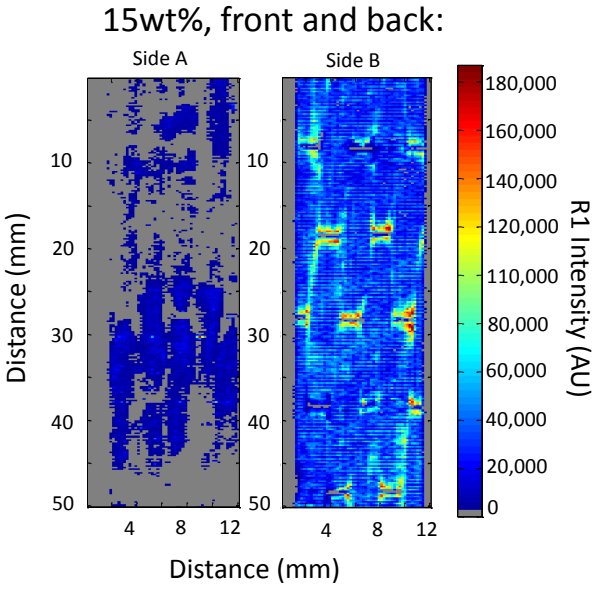

Figure 4.3: Dispersion maps of 15wt% alumina sample

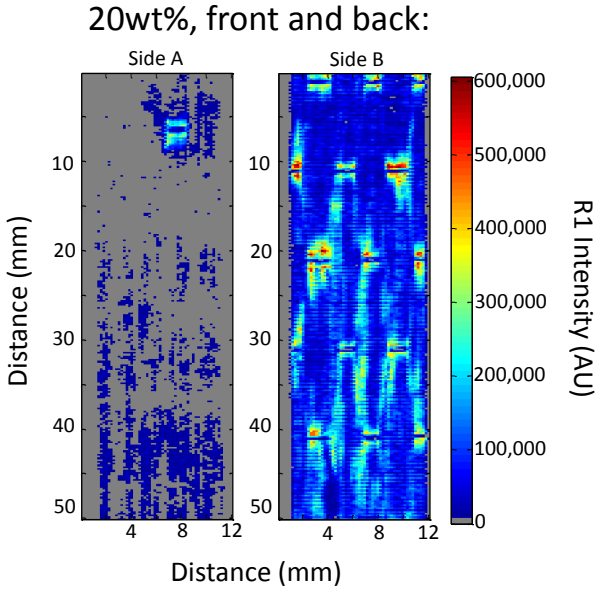

Figure 4.4: Dispersion maps of 20wt% alumina sample

As can be seen in the particulate dispersion maps for the 5 weight percent and 10 weight percent samples in Figure 4.1 and Figure 4.2, the R1 intensity emitted by the embedded particles is relatively uniform throughout the sample. Additionally both the sides of the sample have relatively the same spatial intensity characteristics. Well dispersed particles and low sedimentation are expected in low particulate content composites due to reduced particle-to-particle interaction and enhanced particulate suspension in the matrix epoxy. On the other hand, it can be seen in the dispersion maps for the 15 weight percent and 20 weight percent samples in Figure 4.3 and Figure 4.4 that the spatial intensity varies significantly on each surface, and there are large differences in the front and back sides of the samples. With higher particulate content, this is expected due to increased particle sedimentation to the bottom surface during sample curing.

4.1.2 Agglomeration and Sedimentation Effects

Particle agglomerations, or groups of particles which have collected due to particle-to-particle interactions, are an expected consequence of composites with higher particle contents. Agglomerations introduce non-uniformities in the material, which also produce non-uniformity in the composite's mechanical properties. Additionally, while agglomerations result in higher local intensity, they also result in non-uniform piezospectroscopic stress measurements.

In the photo-luminescent dispersion maps, the particulate agglomerations are represented by higher intensity pixels. These hot-spots of intensity can be seen clearly in the 15 weight percent and 20 weight percent samples in Figures 4.3 and 4.4. Interestingly, the agglomerations are not random, and follow specific spatial location patterns that are consistent with the stitching required in the manufacturing of unidirectional fibrous composites. Due to the predictable and uniform spatial location of agglomerations, it appears that as the resin was being infused into the composite, the particles began to build up at the stitches, which interrupted the resin flow.

To improve settling, a faster curing epoxy may assist by reducing the amount of time the resin is fluid, and restricting the particles movement. Additionally, since stitching is not required for a carbon fiber composite that is +/-45 in it's layout configuration [67], it's therefore likely that agglomerations would be reduced, which could be an interesting area of future work.

Furthermore, the variance in the spatial intensity readings can be well represented in a histogram, which is shown in Figure 4.5 for each sample. In a spatial intensity histogram, the x-axis is the R1 peak intensity, which is an arbitrary unit detected by the charge-coupled device (CCD), and the y-axis is the count of pixels at that specific intensity. An ideal and uniform sample with perfect dispersion would be portrayed as a tall peak with a very narrow full width at half maximum (FWHM). On the other hand, a non-uniform sample would have a short peak with a large FWHM.

A dispersion histogram for each sample at 5, 10, 15, and 20 weight percent alumina is shown in Figure 4.5. Each sample's histogram plot overlays the dispersion histogram of both the front and back side. Additionally, Figure 4.5 shows a global plot which compares the dispersion histograms of all the samples' higher intensity sides.

It can be seen in Figure 4.5 that the 5 and 10 weight percent samples have well dispersed particles, in comparison to the 15 and 20 weight percent samples. Additionally, if two surfaces have the exact same dispersion and no particulate settling, their dispersion histograms would be identical. Therefore, it can be seen in Figure 4.5 that the 5 and 10 weight percent samples have almost no discernible sedimentation, while the higher alumina contents of 15 and 20 weight percent have large settling characterized by the high deviation of each surface's spatial intensity. By changing the alumina particulate content of the resin, the viscosity of the matrix is also changing. This perhaps affects the settling process. Additionally, particle content will also affect the curing time. Arriving at an optimum combination of particulate content, curing time, and matrix viscosity to achieve the best dispersion properties is an interesting area of future investigation, and can be studied through photo-luminescent mapping, as shown in this work.

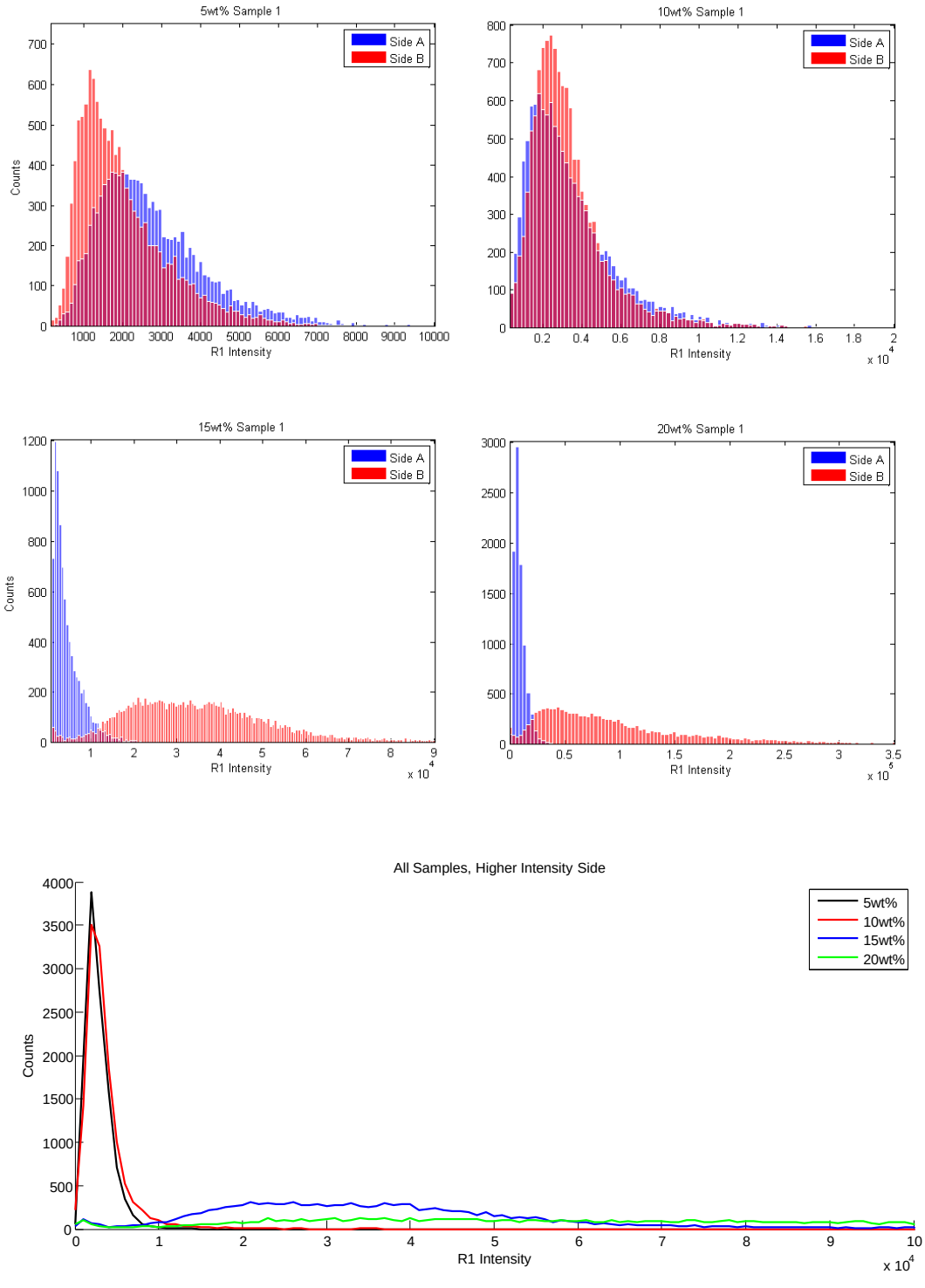

Figure 4.5: Dispersion Analysis Results

In this discussion, the top side refers to the lower intensity side, and the bottom side refers to the higher intensity side, which is where agglomerations are more likely to be present. Since the higher alumina content composites exhibit higher sedimentation, it's important to note that the local alumina content may no longer be the manufactured specific amount. Instead, the top side may have a slightly lower local alumina content, while the bottom side may have a slightly higher alumina content.

While this cannot easily be quantified as a mass or volume content, it can be seen in Figure 4.6 that the top side of the 15 weight percent sample has approximately the same spatial intensity characteristics as the bottom side of the 5 weight percent sample. This indicates that the top surface of the 15 weight percent sample was nearly equivalent in alumina distribution to the bottom surface of the 5 weight percent sample.

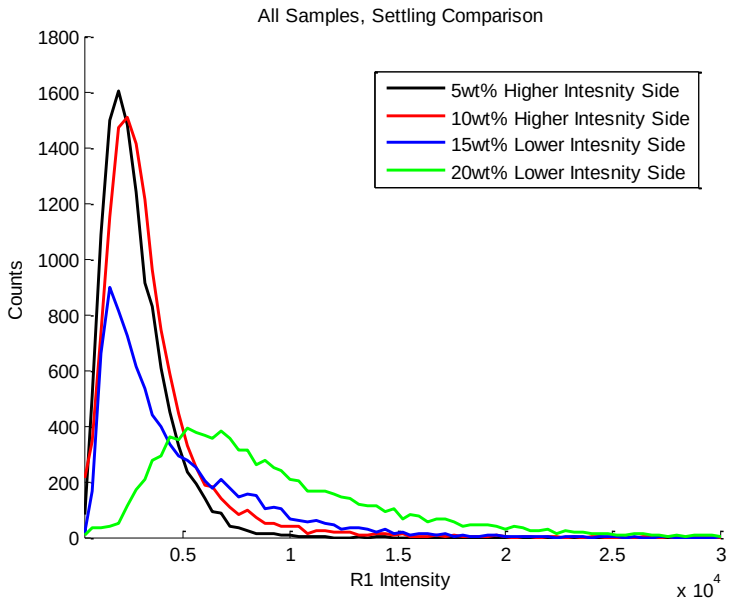

Figure 4.6: Effects of settling histogram

4.1.3 Summary of Particulate Dispersion Results

This study has shown that photo-luminescent spectroscopy can successfully characterize particulate dispersion in a hybrid composite. Although the hybrid composite includes carbon fiber, the intensity from the embedded alumina particles was detectable, and captured a local and global understanding of agglomerations and sedimentation in the hybrid carbon fiber alumina composite.

The 5 and 10 weight percent samples showed excellent dispersion and minimal sedimentation. On the other hand, agglomerations and sedimentation effects were signif-

icantly higher in the 15 and 20 weight percent samples. It was also shown that this technique can predict the local alumina content at the sample's surface. In this work, the top side of the 15 weight percent had almost the same spatial intensity distribution as the bottom side of the 5 weight percent sample. Overall, the implications of this dispersion analysis show that this photo-luminescent mapping procedure has potential for its use as a quality control technique for hybrid composites.

CHAPTER 5
NON-CONTACT STRESS SENSING

In this chapter, the piezosepctroscopic effect is used for non-contact stress sensing of a HCFRP with embedded alumina nanoparticles, and sheds light on the multi-scale mechanics of hybrid composites. The hybrid composites studied here were manufactured with unidirectional fibers and varying alumina contents, in order to study the effects of varying alumina nanoparticles on the stress-sensing ability.

5.1 Stress Mapping

One of the benefits of the piezospectroscopic stress sensing technique is its ability to be utilized *in-situ*. In this study, the testing coupons were subjected to tensile load through a Mechanical Testing System (MTS), and at predetermined static tensile holds, the X-Y-Z stage of the PPS system [34] was used to conduct photo-luminescent maps of each sample's higher SNR side. These photo-luminescent maps were then deconvoluted and post processed using a non-linear least squares curve fitting method in order to track alumina's signature spectral peak shift, which is directly related to stress.

5.1.1 Piezospectroscopic Results

The applied tensile stress was quantified through the average force registered by the MTS load cell at each static hold and the cross sectional area of the sample. At each static hold, a piezospectroscopic map was acquired, and DIC strain images were taken concurrently.

The major benefit of using DIC strain in conjunction with PS mapping is the ability to spatially compare stress and strain. A direct comparison between the PS maps and the DIC maps for the 20 weight percent sample can be found in Figure 5.1. It can be seen that similar trends are present in both, where tensile strain and stress generally increase throughout the sample, with spatial variations present in both the PS maps as well as the DIC maps.

The peak shift trend of the 20 weight percent alumina HCFRP can be seen in Figure 5.2. There is a distinctly linear up-shift region of the R1 peak shift during the ramp-up of the tensile loading, and this linear region appears to become non-linear as the load approaches approximately 250 MPa, or 20% of the estimated ultimate tensile strength [53].

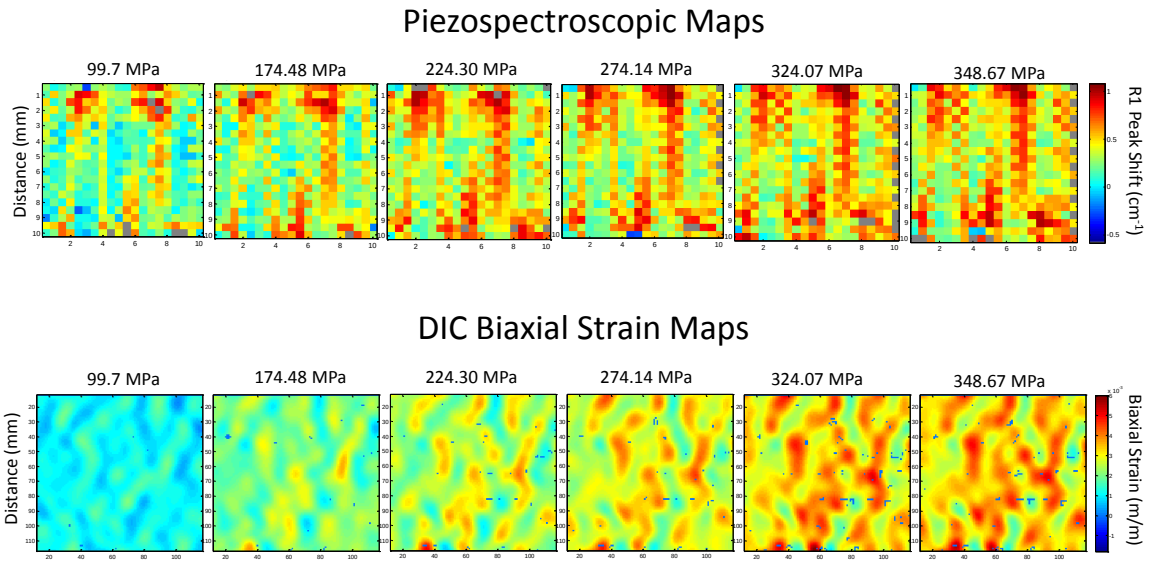

Figure 5.1: PS and DIC maps for 20wt% alumina

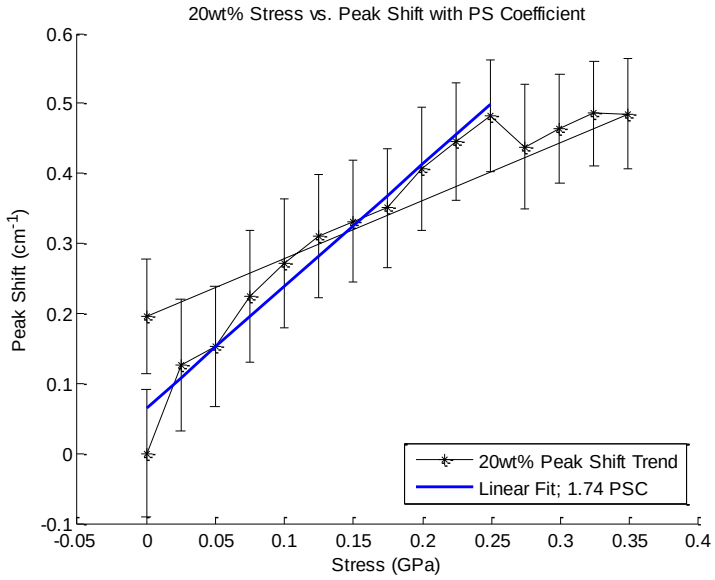

Figure 5.2: Stress-sensing result for the 20wt% sample

The error bars shown in the peak shift trends are a reflectance of spatial variation of the stress in the samples. In other words, agglomerations on the surface result in higher localized volume fractions which are known to experience higher stresses and higher stress sensitivity [65], creating spatial differences in spectral response. Therefore, this expected surface non-uniformity is reflected in the peak shift error bars, and is also later seen in the DIC strain results.

Figure 5.3 shows the stress sensing results of the 15 weight percent alumina HCFRP. The 15 weight percent sample exhibited an initial negative peak shift emitted by the embedded particles at the start of loading. Additionally, the trend for the 15 weight percent sample becomes non-linear at 200 MPa, which is slightly less than the 20 weight percent sample.

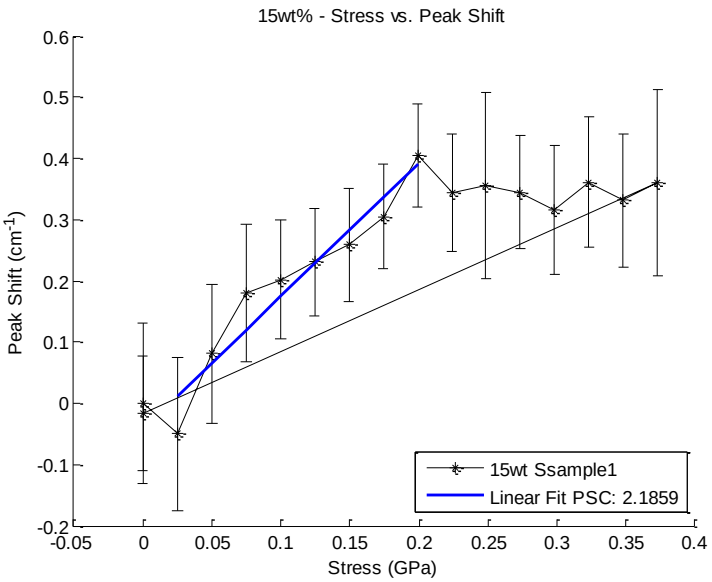

Figure 5.3: Stress-sensing result for the 15wt% sample

The stress sensing results of the 5 weight percent alumina HCFRP are shown in Figure 5.4 and follow a similar trend to the previous samples, showing an initial negative peak shift, a linear ramp to approximately 200 MPa, and then a non-linear region. The slope of the linear region for the 5, 15, and 20 weight percent were calculated as the effective Piezospectroscopic coefficient, and have been plotted in each sample's stress vs. peak shift plot.

The 10 weight percent alumina HCFRP's stress sensing results deviated from the trend of the other samples, and its largely negative peak shift can be seen in the peak shift trend shown in Figure 5.5. This is likely due to moisture ingression, which occurred during the addition of the alumina nanopowder during the manufacturing of the 10 weight percent sample. The reduced load transfer is expected, since moisture ingression has been shown to negatively affect load transfer in composites [43, 1]. This is indicative of the sensitivity of this technique, and its ability to detect manufacturing defects. Therefore, it appears that piezospectroscopy could also be applied to hybrid composites as a crucial quality control step, ensuring the composite's structural properties and integrity.

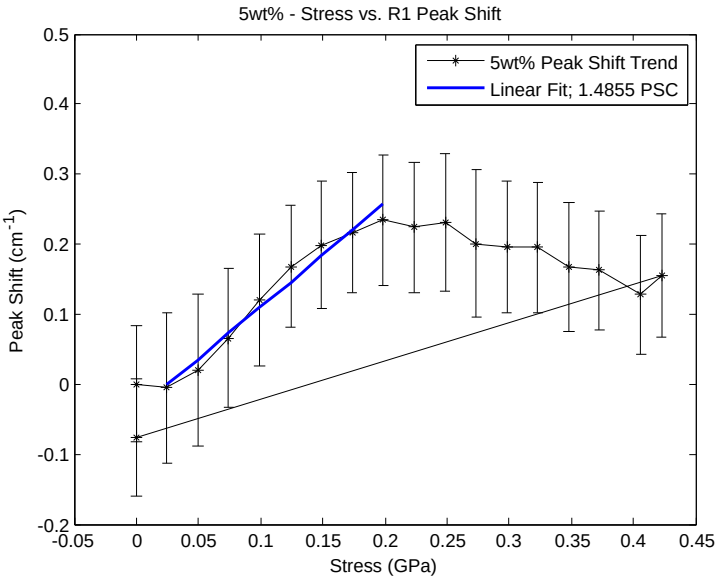

Figure 5.4: Stress-sensing result for the 5wt% sample

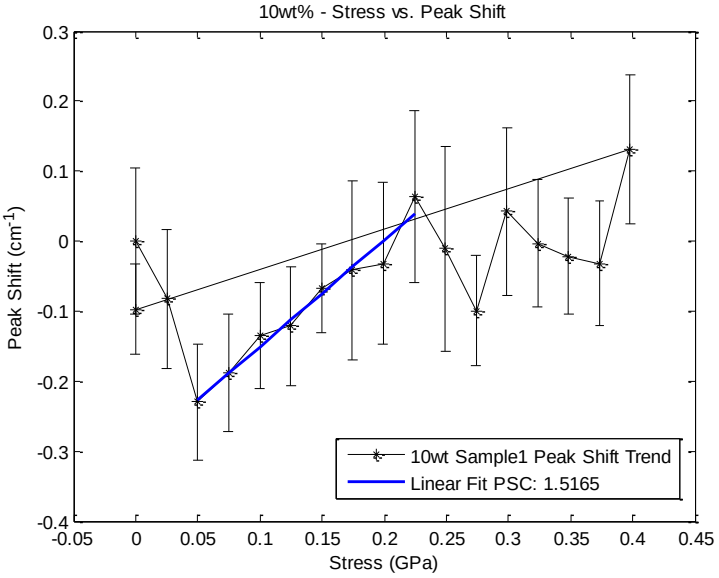

Figure 5.5: Stress-sensing result for the 10wt% sample

5.2 DIC Analysis

The Digital Image Correlation (DIC) analysis was conducted in Vic2d^{TM}, a software that allowed for the inputting of all the images collected as well as a user inputed region of interest. The standard deviation of the strain and peak shift maps was used for the error bars presented in Figures 5.6 through 5.9.

The peak shift in the particles is related to the first strain invariant [22, 35]. In this case, the first strain invariant that the embedded particles experience is directly proportional to the biaxial strain. Therefore, the biaxial strain was chosen as the strain of interest from the DIC maps.

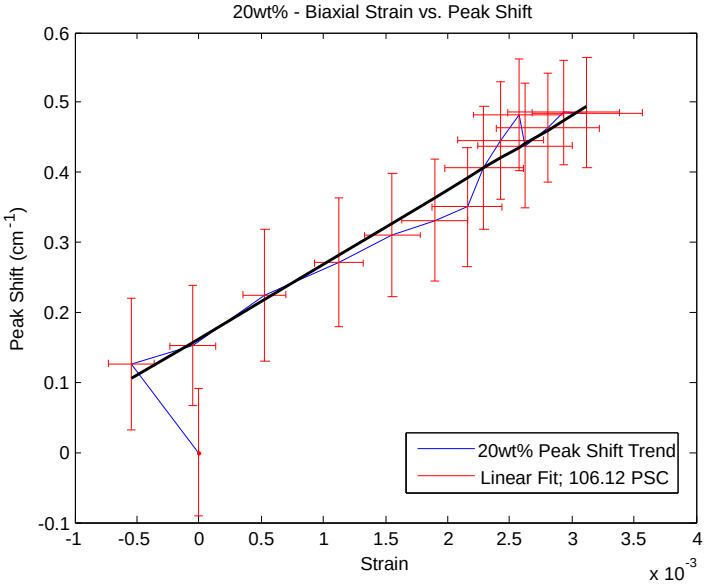

Figure 5.6: DIC biaxial strain vs. peak shift for the 20wt% sample

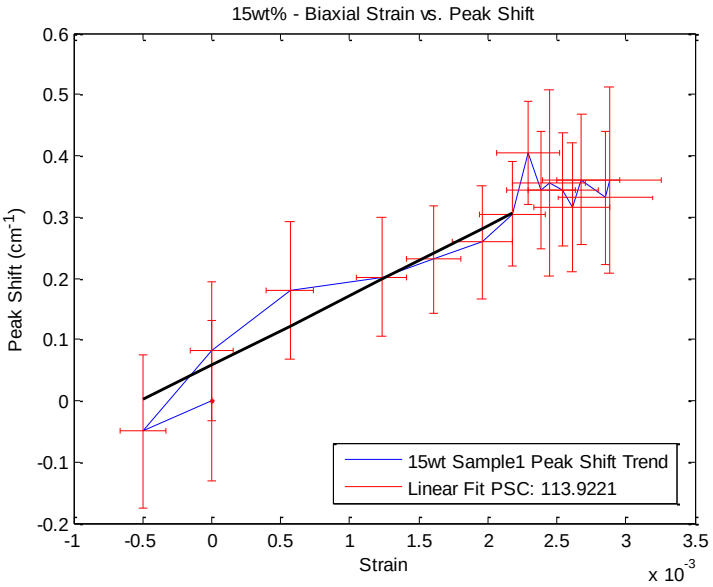

Figure 5.7: DIC biaxial strain vs. peak shift for the 15wt% sample

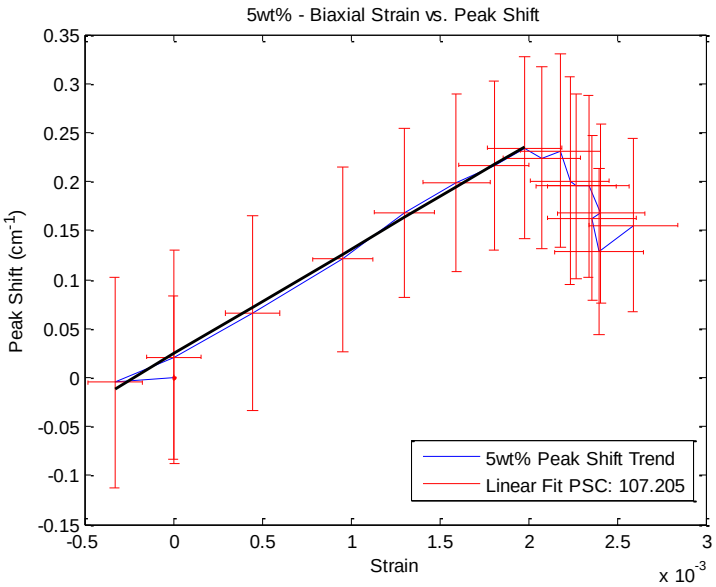

Figure 5.8: DIC biaxial strain vs. peak shift for the 5wt% sample

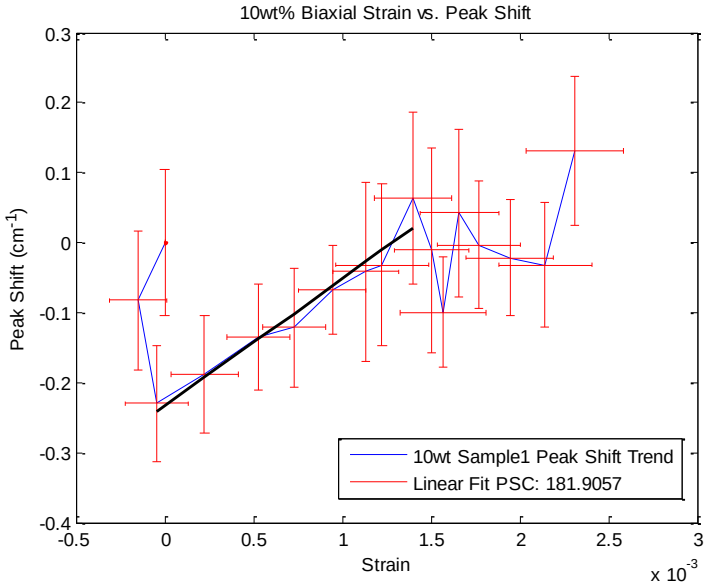

Figure 5.9: DIC biaxial strain vs. peak shift for the 10wt% sample

It can be seen that there is a clearly linear region in all samples when comparing peak shift to DIC strain. At a certain strain, the linear region changes to a very sporadic non-linear trend, which is slightly different for each sample. A global comparison and an explanation for the non-linear behavior is provided below in the discussion.

5.3 Discussion

Discussion of the stress sensing results are presented here, excluding the 10 weight percent alumina sample, which experienced moisture ingression as previously explained. Additionally, an initial analysis of the toughening effects of embedded alumina particles in the HCFRP samples is provided.

5.3.1 Stress Sensing

An important factor of the stress sensing capabilities of this material is its reliability, which can be reflected by the signal to noise ratio (SNR) of the acquired signal. In other words, to ensure the most reliable stress sensing data from the composite, an SNR filter is applied prior to peak-shift processing [34]. The consequence of the SNR filter is that certain pixels of data with low signal intensity are removed, and only high quality signals, with high intensity photo-luminescent peaks, are allowed to continue to the post-processing steps. In Figure 5.10, the zero load map of each sample is shown with an SNR cut off of 25, and as can be seen, the lower alumina contents result in a larger number of gray pixels, which are data points rejected by the SNR filter. This implies that while better dispersion is achieved with lower alumina contents, higher reliability in stress sensing is achieved with higher alumina contents.

In Figure 5.10, it can be seen that the 15 weight percent sample has only a few pixels which passed the SNR filter. This is due to the highly sloped baseline and consequentially lower intensity R-line peaks. During manufacturing, the 15 weight percent sample developed a thin yellow film which is due to non-ideal ventilation conditions in the manufacturing process of that specific sample. While less R-line data points passed the SNR filter, those higher quality R-lines shifted as expected with stress. It appears that the thin yellow film and consequential slanted baseline has a significant effect on the SNR of the data, but not on the peak shift trend. On the other hand, it can be seen that the 10

weight percent sample had overall higher SNR, but experienced moisture ingression and therefore responded unexpectedly to stress. Therefore, while the SNR was higher for the 10 weight percent, the R-line peaks did not shift as expected.

As previously explained, a typical measurement of stress sensing properties of a piezospectroscopic material is the slope of the linear region, known as the piezospectroscopic (PS) coefficient, given in units of cm^{-1}/GPa [65, 22, 35]. The calculated PS coefficients for the 5, 15, and 20 weight percent samples are presented in Table 5.1. It can be seen that the PS coefficient remains relatively constant, and does not discernibly change. Previous work has experimentally shown that adding alumina nanoparticles at high-contents results in an increase in the PS coefficient of a composite [65]. However, it has also been experimentally shown that adding alumina nanoparticles at volume fractions lower that 10% volume content results in insignificant changes in the PS coefficient, which also agreed with theoretical models [22]. Therefore, the equivalent volume contents have also been presented in Table 5.1, and as expected, they are below 10% volume content.

Furthermore, the peak shift data for all three samples offers many insights into the stress sensing phenomenon of the HCFRP composite, as can be seen plotted in Figure 5.11. It is clear that with increased alumina content, there is an increase in the maximum peak shift emitted from the embedded alumina particles. Additionally, it appears that the samples approach a critical stress characterized by a maximum peak shift. From Figure 5.11, it can be seen that the addition of alumina particles results in a larger

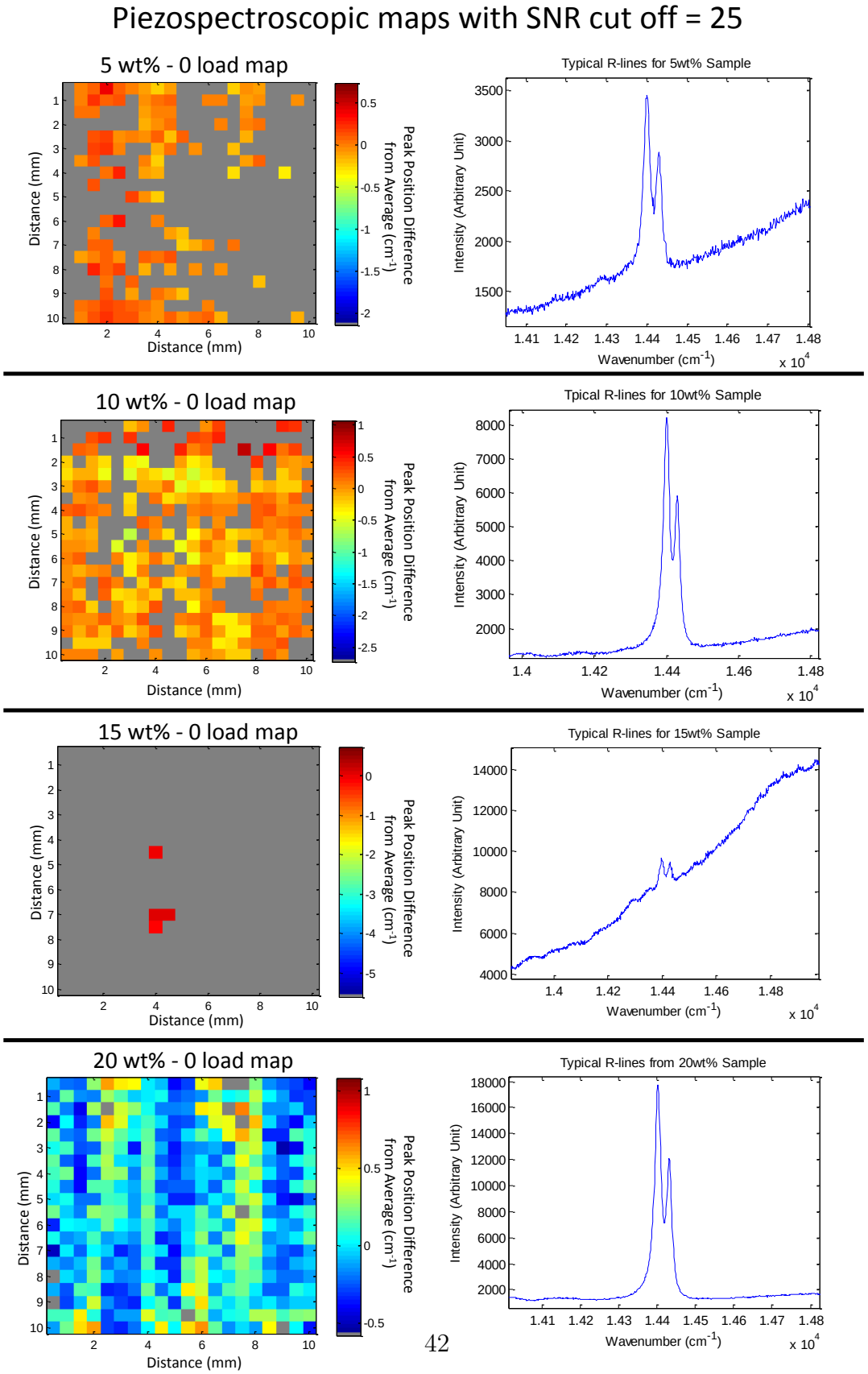

Figure 5.10: Signal-to-Noise Ratio of PS maps

Table 5.1: PS Coefficients of HCFRP with varying alumina contents

Alumina Weight Content	Equivalent Volume Content	Experimental HCFRP PS Coefficient (cm^{-1}/GPa)
5%	1.57%	1.49 ± 0.53
15%	5.07%	2.19 ± 0.62
20%	7.03%	1.74 ± 0.34

critical stress. Specifically, the 5, 15, and 20 weight percent samples appear to approach a maximum critical stress of approximately 213, 275, and 350 MPa, respectively. This critical stress point is hypothesized to be the particle-matrix debonding point, or the point at which the particle-matrix interface is permanently damaged and consequentially decreases the load transfer from the matrix to the particle [23].

Comparing the unloading curves shown in Figure 5.11 also sheds light on the effects of the critical stress. The 20 weight percent sample does not yet reach the maximum peak shift at its critical stress, and unloads to a positive, or tensile, peak shift. The 15 weight percent appears to reach a maximum peak shift point without surpassing its critical stress, and unloads to a nearly 0 peak shift. Lastly, the 5 weight percent reaches and surpasses its critical stress, as can be seen in Figure 5.11, and consequentially unloads to a negative, or compressive, peak shift. Therefore, it appears that by measuring the peak shift after a cycle of loading, it can be determined whether the sample reached, or surpassed, its critical stress point, hypothesized to be the particulate debonding point.

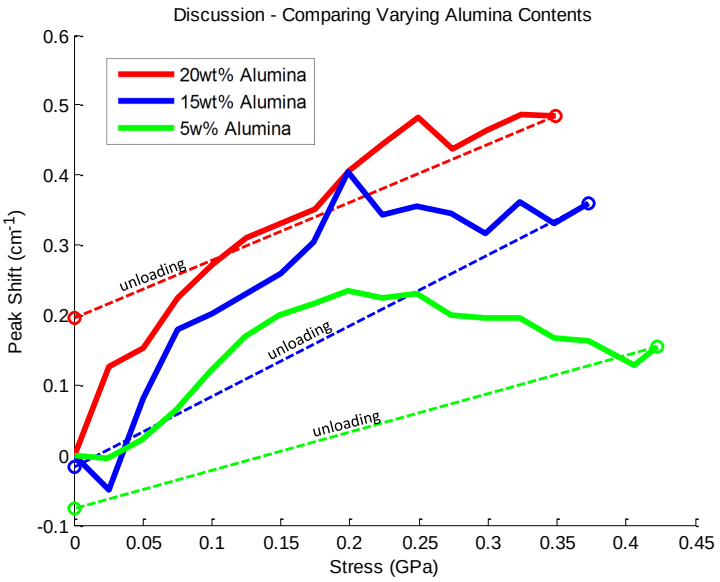

Figure 5.11: Comparing stress vs. peak shift for the 5, 15, and 20 weight percent

Similar to the stress vs. peak shift result, the 5, 15, and 20 weight percent peak shift trends with respect to strain can be compared in Figure 5.12. Similarly, a linear region can be seen during ramp-up, and the slope can be calculated as the strain-based PS coefficient, given in Table 5.2. As expected, due to the low volume content of the alumina, the PS coefficients do not discernibly increase with increasing alumina content.

One interesting phenomenon seen in the strain results is the trend of peak shift after the critical point. While all alumina contents are approaching a maximum peak shift at the critical strain, the strain behavior after the critical point is very different in each sample. It appears that the higher alumina contents exhibit a more resilient, positively sloped peak shift trend after the critical strain, whereas the 5 weight percent alumina appears to quickly drop in peak shift with respect to strain. This could be due to the

increased particle-particle and particle-fiber interactions occurring with higher alumina contents.

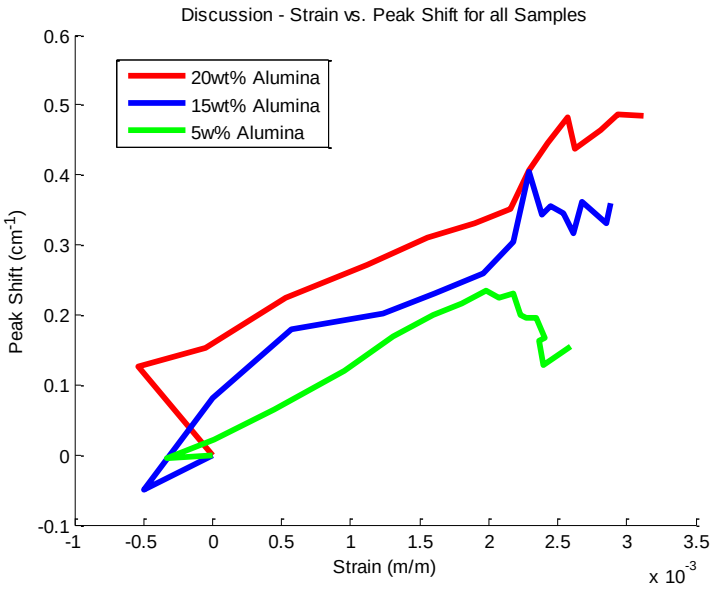

Figure 5.12: Comparing strain vs. peak shift for the 5, 15, and 20 weight percent

Table 5.2: Strain based PS coefficients

Alumina weight content	Strain PS Coefficient $(cm^{-1}/(m/m))$
5	106.12 ± 21.7
15	113.92 ± 41.8
20	107.21 ± 21.6

5.3.2 Toughening

It was previously mentioned that the addition of ceramic particulate fillers, such as alumina, introduce improved toughness in the composite. Traditionally, the tensile toughness of a material is computed as the integral of the stress-strain curve from 0 load until failure. The experiments conducted on the HCFRP samples were non-destructive, and therefore, data until failure was not collected.

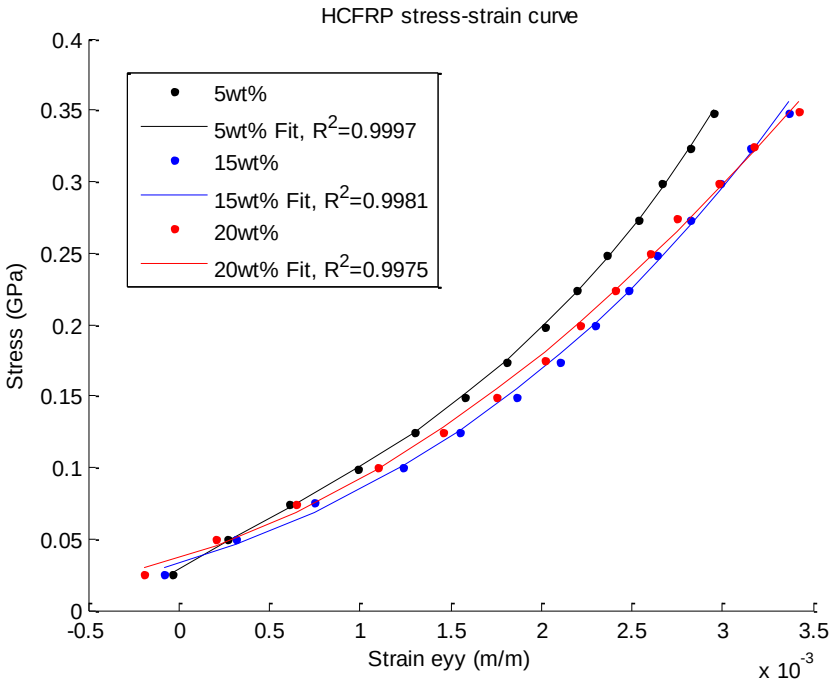

Figure 5.13: The partial stress-strain curve of each HCFRP sample

The partial stress-strain profiles can be used to predict whether the composites show signs of increased toughness. The stress-strain curves of the 5, 15 and 20 weight percent

alumina samples can be seen in Figure 5.13, plotted up to 350 MPa, which was achieved for all samples.

By integrating the partial stress-strain curve, a partial toughness can be calculated. The partial tensile toughness is inconclusive of the true tensile toughness, and cannot be used as an absolute measure of toughness. However, it can be used to predict whether an increase in toughness will be present in the HCFRP samples with increasing alumina. As can be seen in Table 5.3, there does appear to be an increase in partial toughness with increasing alumina content. In order to be conclusive, the toughness must be calculated until fracture, and therefore this is an important area of future work.

Table 5.3: Partial tensile toughness of each HCFRP sample

Weight Percent Alumina	Partial Tensile Toughness (kJ/m^3)
5%	465.7834
15%	530.0306
20%	573.6757

5.4 Summary of Results

Overall, it was shown that piezospectroscopic mapping can be used to monitor stress evolution in an alumina HCFRP, which high spatial resolution and *in-situ* capabilities. There appears to be systematic trends in stress vs. peak shift, which are complimented

by the DIC strain vs. peak shift results. While there was a higher magnitude of peak shift with increasing alumina content, there did not appear to be an increase in PS coefficient, which is expected for low volume fractions of alumina.

With lower alumina contents, it was clear that there was a drop in signal-to-noise ratio. Additionally, it was seen that piezospectroscopic mapping is capable of detecting manufacturing irregularities, such as moisture ingression in the 10 weight percent sample.

One key result was the critical stress point, which is thought to be the point at which the particule debonds from the matrix, characterized by a maximum peak shift followed by a drop in peak shift. This also implies that a photo-luminescent map of the HCFRP's surface after a cycle can reveal whether the composite reached or surpassed its critical stress point.

Lastly, preliminary analysis of the toughening effects of alumina particles in an HCFRP composite predict that there will indeed be an increase in toughness due to the particulate inclusion, as expected. However, future work will experimentally determine the true tensile toughness in order to conclusively determine the increase in toughness due to additional alumina nanoparticles.

CHAPTER 6
CONCLUSION

This work investigated the stress sensing capabilities of a hybrid carbon fiber reinforced polymer (HCFRP) with embedded alumina nanoparticles. The samples were manufactured through a procedure known as resin infusion under flexible tooling (RIFT), which utilizes a vacuum reservoir to draw the epoxy-alumina matrix around the uni-directional carbon fibers.

Photo-luminescent intensity maps were used to quantify particulate dispersion in the top and bottom side of each sample. Sedimentation was quantified to be significantly higher for the 15 and 20 weight percent alumina, while minimal sedimentation was observed in the 5 and 10 weight percent alumina. These dispersion results can aid in manufacturing improvements, and show that this technique can provide high spatial resolution quality control for future implementation in structures.

The stress sensing capability made possible by the piezospectroscopic effect, a phenomenon in which the emitted photo-luminescent (PL) spectrum of a material shifts as the material is stressed, was also investigated in this work. By utilizing the embedded alumina particles' piezospectroscopic properties, non-contact stress sensing was achieved.

The resulting piezospectroscopic maps showed stress trends that matched well with DIC strain maps, and showed a linear ramp-up in peak shift as increased stress was applied, until a maximum peak shift was achieved at a critical stress. This critical stress varied between each sample, and increases with increasing alumina content.

Unloading curves proved to be dependent on whether the sample reached its critical stress, or surpassed its critical stress. It appears that if the sample is unloaded prior to reaching the critical stress, it will unload to a positive, or tensile, peak shift. On the other hand, if it reaches and surpasses its critical stress, it will unload to a negative, or compressive, peak shift. The experimentally measured critical stress point is hypothesized to be the particle-matrix debonding point, after which the peak shift appears to decrease. The ability to measure the debonding point can allow for experimental analysis on how different surface treatments of nanoparticles impact the particle-matrix interface, *in-situ*. Furthermore, the debonding point provides an additional measure of material performance, and can help guide the future implementation of this HCFRP composite.

Overall, this work introduced a novel approach to stress sensing of a hybrid composite, which has light weight, and high performing mechanical properties, as well as an inherent non-contact stress sensing capability. The results presented in this work hold implications for the future of non-destructive inspection and non-contact damage detection, which will lend itself to more precise measurements with high spatial resolution. Future work will aim to characterize the full mechanical properties of this HCFRP, including it's true toughness. Additionally, the critical stress point will be further explored in order to understand the micromechanics of the particle, matrix, and fiber interfacial responses.

LIST OF REFERENCES

[1] M. Akay, S. K. A. Mun, and A. Stanley. Influence of moisture on the thermal and mechanical properties of autoclaved and oven-cured kevlar-49/epoxy laminates. *Composites science and technology*, 57(5):565–571, 1997.

[2] A. Alva and S. Raja. Dynamic characteristics of epoxy hybrid nanocomposites. *Jounal of Reinforced Plastics and Composites*, 30 (22):1857, 2011.

[3] M. Arroyo and F. Avalos. Polypropylene/low density polyethylene blend matrices and short glass fibers based composites. i. mechanical degradation of fibers as a function of processing method. *Polymer composites*, 10(2):117–121, 1989.

[4] ASTM. D3039/d3039m-00. *Standard test method for tensile properties of polymer matrix composite materials*, 2000.

[5] I. D. Baere, W. V. Paepegem, and J. Degrieck. On the design of end tabs for quasi-static and fatigue testing of fibre-reinforced composites. *Polymer Composites*, 10:381–390, 2009.

[6] S. Bagavathiappan, B. Lahiri, T. Saravanan, J. Philip, and T. Jayakumar. Infrared thermography for condition monitoring–a review. *Infrared Physics & Technology*, 60:35–55, 2013.

[7] J. D. Barnett, S. Block, and G. J. Piennarini. An optical fluorescence system for quantitative pressure measurement in the diamond-anvil cell. *The Review of Scientific Instruments*, 44:1–9, 1973.

[8] R. S. Bay. *Fiber orientation in injection-molded composites: A comparison of theory and experiment*. PhD thesis, University of Illinois at Urbana-Champaign, 1991.

[9] J.-M. Berthelot. Transverse cracking and delamination in cross-ply glass-fiber and carbon-fiber reinforced plastic laminates: static and fatigue loading. *Applied Mechanics Reviews*, 56(1):111–147, 2003.

[10] J. Chervin, B. Canny, and M. Mancinelli. Ruby-spheres as pressure gauge for optically transparent high pressure cells. *High Pressure Research*, 21:305–314, 2001.

[11] R. Christensen, D. Lipkin, and D. Clarke. Nondestructive evaluation of the oxidation stresses through thermal barrier coatings using Cr^{3+} piezospectroscopy. *Applied Physics Letters*, 69:3754–3756, 1996.

[12] T. Chu, W. Ranson, and M. Sutton. Applications of digital-image-correlation techniques to experimental mechanics. *Experimental mechanics*, 25(3):232–244, 1985.

[13] D. Clarke, R. Christensen, and V. Tolpygo. Evolution of oxidation stresses in zirconia thermal barrier coated superalloy leading to spalling failure. *Surface Coatings and Technology*, 94-95:89–93, 1997.

[14] J. Denault, T. Vu-Khanh, and B. Foster. Tensile properties of injection molded long fiber thermoplastic composites. *Polymer Composites*, 10(5):313–321, 1989.

[15] B. W. Drinkwater and P. D. Wilcox. Ultrasonic arrays for non-destructive evaluation: A review. *Ndt & E International*, 39(7):525–541, 2006.

[16] R. Forman, G. Piermarini, J. Barnett, and S. Block. Pressure measurement made by the utilization of ruby sharp-line luminescence. *Science*, 176(4032):284–285, 1972.

[17] D. Francis, R. Tatam, and R. Groves. Shearography technology and applications: a review. *Measurement science and technology*, 21(10):102001, 2010.

[18] B. Franzen, C. Klason, J. Kubat, and T. Kitano. Fibre degradation during processing of short fibre reinforced thermoplastics. *Composites*, 20(1):65–76, 1989.

[19] G. Freihofer, A. Bullock, F. Vaughn, H. Tat, J. Dustin, A. Schülzgen, and S. Raghavan. Stress and damage sensing of composite coupons with piezospectroscopic coatings. Seattle, WA, 2-5 June 2014. Society for the Advancement of Material and Process Engineering.

[20] G. Freihofer, J. Dustin, H. Tat, A. Schülzgen, and S. Raghavan. Stress and structural damage sensing piezospectroscopic coatings validated with digital image correlation. *AIP Advances*, 5(3):037139, 2015.

[21] G. Freihofer, D. Fugon-Dessources, E. Ergin, A. V. Newkirk, A. Gupta, S. Seal, A. Schülzgen, and S. Raghavan. Piezospectroscopic measurements capturing the evolution of plasma-spray coating stresses with substrate loads. *ACS Applied Materials & Interfaces*, 6(3):1366–1369, 2014.

[22] G. Freihofer, A. Schülzgen, and S. Raghavan. Multiscale mechanics to determine nanocomposite elastic properties with piezospectroscopy. *Acta Materialia*, 81:211–218, 2014.

[23] Fu, Feng, Lauke, and Mai. Effects of particle size, particle/matrix interface adhesion and particle loading on mechanical properties of particulatepolymer composites. *Composites: Part B*, 39:933–961, 2008.

[24] S. Fu, B. Lauke, E. Mäder, X. Hu, and C. Yue. Fracture resistance of short-glass-fiber-reinfored and short-carbon-fiber-reinforced polypropylene under charpy impact load and its dependence on processing. *Journal of Materials Processing Technology*, 89:501–507, 1999.

[25] S.-Y. Fu and B. Lauke. Effects of fiber length and fiber orientation distributions on the tensile strength of short-fiber-reinforced polymers. *Composites Science and Technology*, 56(10):1179–1190, 1996.

[26] S.-Y. Fu, B. Lauke, E. Mäder, C.-Y. Yue, and X. Hu. Tensile properties of short-glass-fiber-and short-carbon-fiber-reinforced polypropylene composites. *Composites Part A: Applied Science and Manufacturing*, 31(10):1117–1125, 2000.

[27] S.-Y. Fu, Y.-W. Mai, E. C.-Y. Ching, and R. K. Li. Correction of the measurement of fiber length of short fiber reinforced thermoplastics. *Composites Part A: Applied Science and Manufacturing*, 33(11):1549–1555, 2002.

[28] G. T. Furukawa, T. B. Douglas, R. E. McCoskey, and D. C. Ginnings. Thermal properties of aluminum oxide from 0 K to 1200 K. *J Res Nat Bur Stand*, 57(2):67–82, 1956.

[29] M. Gallas, Y. Chu, and G. Piermarini. Calibration of the raman effect in α-Al_2O_3 ceramic for residual stress measurements. *Journal of Materials Reseach*, 10(11):2817–2822, 1995.

[30] M. Gell, S. Sridharan, and M. Wen. Photoluminescence piezospectroscopy a multi purpose quality control and NDI technique for thermal barrier coatings. *International Journal of Applied Ceramics Technology*, 1(4):316–329, October 2004.

[31] S. Ghiorse. Effect of void content on the mechanical properties of carbon/epoxy laminates. *SAMPE quarterly*, 24(2):54–59, 1993.

[32] W. H. Gitzen. Alumina as a ceramic material. 1970.

[33] L. Grabner. Spectroscopic technique for the measurement of residual stress in sintered Al_2O_3. *Journal of Applied Physics*, 49:580–583, 1978.

[34] I. Hanhan, E. Durnberg, G. F. P. Akin, and S. Raghavan. Portable piezospectroscopy system: non-contact in-situ stress sensing through high resolution photo-luminescent mapping. *Journal of Instrumentation*, 9(11):P11005, 2014.

[35] J. He and D. R. Clarke. Determination of the piezospectroscopic coefficients for chromium doped sapphire. *Journal of American Ceramic Society*, 78(5):1347–1353, 1995.

[36] F. Henning, H. Ernst, and R. Brüssel. LFTs for automotive applications. *Reinforced plastics*, 49(2):24–33, 2005. LFTs for car industry.

[37] T. M. Hermann, J. E. Locke, and K. K. Wetzel. Fabrication, testing, and analysis of anisotropic carbon/glass hybrid composites volume 1: Technical report. Technical report, Sandia National Laboratories, November 2006.

[38] H. Hough, J. Demas, T. Williams, and H. Wadley. Luminescence sensing of stress in Ti/Al_2O_3 fiber reinforced composites. *Acta metallurgica et materialia*, 43(2):821–834, 1995.

[39] T. Hsieh, A. Kinloch, K. Masania, J. S. Lee, A. Taylor, and S. Sprenger. The toughness of epoxy polymers and fibre composites modified with rubber microparticles and silica nanoparticles. *Journal of materials science*, 45(5):1193–1210, 2010.

[40] M. Hussain, A. Nakahira, and K. Niihara. Mechanical property improvement of carbon fiber reinforced epoxy composites by Al_2O_3 filler dispersion. *Materials Letters*, 26(3):185–191, 1996.

[41] Inframat®. Material specifications of α-Al_2O_3. Web.

[42] D. C. J.A. Nychka. Damage quantification in TBCs by photo-stimulated luminescence spectroscopy. *Surface Coatings and Technology*, 146-147:110–116, 2001.

[43] B. G. Kumar, R. P. Singh, and T. Nakamura. Degradation of carbon fiber-reinforced epoxy composites by ultraviolet radiation and condensation. *Journal of Composite Materials*, 36(24):2713–2733, 2002.

[44] Q. Ma and D. Clarke. Piezospectroscopic determination of residual stresses in polycrystalline alumina. *Journal of American Ceramic Society*, 77:298–302, 1994.

[45] Q. Ma and D. R. Clarke. Stress measurement in single-crystal and polycrystalline ceramics using their optical fluorescence. *Journal of the American Ceramic Society*, 76(6):1433–1440, 1993.

[46] C. Manjunatha, R. Bojja, N. Jagannathan, A. Kinloch, and A. Taylor. Enhanced fatigue behavior of a glass fiber reinforced hybrid particles modified epoxy nanocomposite under wisperx spectrum load sequence. *International Journal of Fatigue*, 54:25–31, 2013.

[47] N. McCormick and J. Lord. Digital image correlation. *Materials today*, 13(12):52–54, 2010.

[48] A. Mohanty, V. K. Srivastava, and P. U. Sastry. Investigation of mechanical properties of alumina nanoparticle-loaded hybrid glass/carbon-fiber-reinforced epoxy composites. *Journal of Applied Polymer Science*, 131(1), 2014.

[49] S. Molis and D. Clarke. Measurement of stresses using fluorescence in an optical microprobe: Stresses around indentations in a chromium-doped sapphire. *Journal of Electronic Structure of Ceramics*, 73(11):3189 –3194, 1990.

[50] M. MUNRO. Evaluated material properties for a sintered alpha-alumina. *Journal of the American Ceramic Society*, 80(8):1919–1928, 1997.

[51] B. N. Nguyen, S. K. Bapanapalli, J. D. Holbery, M. T. Smith, V. Kunc, B. J. Frame, J. H. Phelps, and C. L. Tucker. Fiber length and orientation in long-fiber injection-molded thermoplasticspart i: Modeling of microstructure and elastic properties. *Journal of composite materials*, 42(10):1003–1029, 2008.

[52] J. Njuguna, K. Pielichowski, and J. R. Alcock. Epoxy-based fibre reinforced nanocomposites. *Advanced Engineering Materials*, 10:835–847, 2007.

[53] J. M. F. d. Paiva, S. Mayer, and M. C. Rezende. Comparison of tensile strength of different carbon fabric reinforced epoxy composites. *Materials Research*, 9(1):83–90, 2006.

[54] J. H. Phelps. *Processing-microstructure models for short-and long-fiber thermoplastic composites*. PhD thesis, University of Illinois at Urbana-Champaign, 2009.

[55] J. H. Phelps and C. L. Tucker. An anisotropic rotary diffusion model for fiber orientation in short-and long-fiber thermoplastics. *Journal of Non-Newtonian Fluid Mechanics*, 156(3):165–176, 2009.

[56] G. J. Piermarini, S. Block, J. D. Barnett, and R. A. Forman. Calibration of the pressure dependence of the R1 ruby fluorescence line to 195 kbar. *Journal of Applied Physics*, 46:2774, 1975.

[57] S. Raghavan and P. Imbrie. The development of photo-stimulated luminescence spectroscopy for 3D stress measurements in the thermally grown oxide layer of thermal barrier coatings. In *Proceedings of the Materials Science and Technology 2007 conference*, 2007.

[58] S. Raghavan, A. Stevenson, and A. Jones. Stress-sensitive material and methods for using same, Sept. 28 2012. US Patent Pub. No. 20130082191A1.

[59] G. S. Rellick, R. J. Zaldivarz, and P. M. Adams. Fiber-matrix interphase development in carbon/carbon composites. Technical report, Mechanics and Materials Technology Center Technology Operations, 1998.

[60] R. Sampaio, N. Maia, and J. Silva. Damage detection using the frequency-response-function curvature method. *Journal of Sound and Vibration*, 226(5):1029–1042, 1999.

[61] S. Saunders, J. Banks, G. Chen, and C. Chunnilal. Measurement of residual stress in thermally grown oxide layers in thermal barrier coating systems - development of non-destructive test methods. *Materials Science Forum*, 461-464:383–390, 2004.

[62] R. Selzer and K. Friedrich. Mechanical properties and failure behaviour of carbon fibre-reinforced polymer composites under the influence of moisture. *Composites Part A: Applied Science and Manufacturing*, 28(6):595–604, 1997.

[63] C. Soutis. Carbon fiber reinforced plastics in aircraft construction. *Materials Science and Engineering*, A 412:171176, 2005.

[64] A. Stevenson, A. Jones, and S. Raghavan. Characterization of particle dispersion and volume fraction in alumina-filled epoxy nanocomposites using photo-stimulated luminescence spectroscopy. *Polymer journal*, 43(11):923–929, 2011.

[65] A. Stevenson, A. Jones, and S. Raghavan. Stress-sensing nanomaterial calibrated with photostimulated luminescence emission. *Nano letters*, 11(8):3274–3278, 2011.

[66] I. Trendafilova, M. Cartmell, and W. Ostachowicz. Vibration-based damage detection in an aircraft wing scaled model using principal component analysis and pattern recognition. *Journal of Sound and Vibration*, 313(3):560–566, 2008.

[67] T. C. Truong, M. Vettori, S. Lomov, and I. Verpoest. Carbon composites based on multi-axial multi-ply stitched preforms. part 4. mechanical properties of composites and damage observation. *Composites Part A: applied science and manufacturing*, 36(9):1207–1221, 2005.

[68] T. Vu-Khanh, J. Denault, P. Habib, and A. Low. The effects of injection molding on the mechanical behavior of long-fiber reinforced PBT/PET blends. *Composites science and technology*, 40(4):423–435, 1991.

[69] J. C. Williams and E. A. Starke. Progress in structural materials for aerospace systems. *Acta Materialia*, 51(19):5775–5799, 2003.

[70] Y. Xu and S. Van Hoa. Mechanical properties of carbon fiber reinforced epoxy/clay nanocomposites. *Composites Science and Technology*, 68(3):854–861, 2008.

[71] Y. Zheng and R. Ning. Study of SiO_2 nanoparticles on the improved performance of epoxy and fiber composites. *Journal of Reinforced Plastics and Composites*, 24:223, 2005.

[72] Y. Zou, L. Tong, and G. Steven. Vibration-based model-dependent damage (delamination) identification and health monitoring for composite structuresa review. *Journal of Sound and vibration*, 230(2):357–378, 2000.